ChemCatChem

ChemCatChem
Chemistry Europe
European Chemical Societies Publishing

RESEARCH ARTICLE OPEN ACCESS

Coupled Operando Mössbauer-Raman Spectroscopic Analysis of Iron Molybdate Catalysts During Oxidative Dehydrogenation

Lanjie Jiang[1] | Jan Welzenbach[1] | Jonas Spielmann[1] | Hannah M. Wilhelm[1] | Kathrin Hofmann[1] | Felix Reinauer[1] | Jan-Dierk Grunwaldt[2] | Barbara Albert[3] | Christian Hess[1] | Ulrike I. Kramm[1]

[1]Department of Chemistry, Eduard-Zintl-Institute of Inorganic and Physical Chemistry, Technische Universität Darmstadt, Darmstadt, Germany | [2]Institute for Chemical Technology and Polymer Chemistry (ITCP) and Institute of Catalysis Research and Technology (IKFT), Karlsruhe Institute of Technology (KIT), Karlsruhe, Germany | [3]University of Duisburg-Essen, Essen, Germany

Correspondence: Christian Hess (christian.hess@tu-darmstadt.de) | Ulrike I. Kramm (ulrike.kramm@tu-darmstadt.de)

Received: 28 January 2026 | **Revised:** 12 May 2026 | **Accepted:** 23 June 2026

Keywords: In situ/operando spectroscopy | Raman spectroscopy | Mössbauer spectroscopy | catalysis | oxidative dehydrogenation | iron molybdate | oxygen transport | redox

ABSTRACT

Coupling operando synchrotron-based Mössbauer spectroscopy (SMS) with operando Raman spectroscopy provides complementary structural information during catalytic reactions. We demonstrate the potential of this approach for the oxidative dehydrogenation of ethanol to acetaldehyde over an iron molybdate catalyst. The coupled SMS-Raman approach enables the simultaneous detection of bulk (^{57}Fe Mössbauer) and (sub)surface (Raman) structural changes and their correlation with the catalytic conversion and selectivity recorded by online mass spectrometry. Based on the high photon flux at the synchrotron and absence of a non-resonant background, SM spectra could be recorded with high time resolution, enabling simultaneous analysis by SMS and Raman spectroscopy. Exposure to reducing conditions (absence of gaseous oxygen), while the reaction to acetaldehyde is maintained, revealed a significantly faster response of Raman signals from crystalline phases (MoO_3, $Fe_2(MoO_4)_3$) in comparison to SMS, which originates from the higher surface sensitivity of Raman spectroscopy. SMS as a bulk technique monitors the reduction of iron, leading to β-$FeMoO_4$ formation under reductive conditions. Our results show that the application of coupled (sub)surface and bulk operando methods strongly facilitates a detailed understanding of the structure-activity relationship of bulk metal oxide catalysts in selective oxidation reactions, including oxygen transport from the bulk to the catalyst surface.

1 | Introduction

Iron(III) molybdate ($Fe_2(MoO_4)_3$)-based catalysts represent the state-of-the art material for oxidative dehydrogenation (ODH) of methanol to formaldehyde [1]. For industrial applications, the catalyst is usually applied with an excess of MoO_3 to improve the selectivity and stability [2]. In a recent work, Oefner et al. showed that the same material is also very active and selective for the ethanol (EtOH) ODH to acetaldehyde [3]. For both reactions, ODH of methanol and ethanol, a Mars-van Krevelen mechanism has been proposed, similar to other selective oxidation reactions [4–6]. This means that during the reaction, lattice oxygen reacts with the substrate (e.g., methanol or ethanol), followed by the replenishment of anion vacancies by oxygen from the gaseous

Lanjie Jiang and Jan Welzenbach have contributed equally to this work.

feed. Depending on the kinetics of both steps, this can cause a more or less pronounced reduction of the transition metals. In an in situ x-ray absorption spectroscopy (XAS) study combined with x-ray diffraction (XRD) structural changes were monitored during redox cycling on $Fe_2(MoO_4)_3$ with excess MoO_3 (Mo:Fe = 2) [7]. It was shown that upon heating from 100°C to 400°C, the catalyst was reduced to Mo(IV) and Fe(II), forming MoO_2 and $FeMoO_4$ when gaseous oxygen was absent (5% MeOH/He). Subsequent oxidation (10% O_2/He) between 200°C and 500°C returned the catalyst to its original state, involving intermediate phases of Fe_2O_3 and extra MoO_3. On the basis of in situ wide-angle x-ray scattering (WAXS), XAS, and UV-Vis spectroscopy on stoichiometric $Fe_2(MoO_4)_3$ in methanol ODH, it was concluded that $Fe_2(MoO_4)_3$ is transformed under reductive conditions first to an oxygen-deficient intermediate (named P1) and then to β-$FeMoO_4$ and a MoC-type phase (P2) [8].

More relevant information can be extracted from operando spectroscopies, in which the conversion and selectivity are measured in parallel to the spectroscopic changes. Using operando synchrotron XAS/XRD and operando Raman spectroscopy on a mixed $MoO_3/Fe_2(MoO_4)_3$ catalyst (Mo:Fe = 2), the loss of excess α-MoO_3 under reactive conditions was detected and related to the observed decrease in performance [9]. The authors proposed that the presence of an excess of α-MoO_3 minimizes the reduction of $Fe_2(MoO_4)_3$. Using a combination of operando UV-Vis, UV Raman, and impedance spectroscopy as well as transient IR spectroscopy during propane ODH over $Fe_2(MoO_4)_3$, it was shown that molybdenyl (Mo = O) containing surface species act as active redox sites and that the presence of iron supports the oxygen transport by influencing oxygen diffusion within the catalyst [10]. Bates performed anaerobic titration experiments coupled with x-ray absorption techniques and showed that the removable oxygen species, which are active in the reaction, are shared between Fe and Mo within the $Fe_2(MoO_4)_3$ lattice [11]. This finding underscores the importance of the role of iron molybdate in facilitating the ODH process. While there were different conclusions on the role of molybdenum oxide, it is evident that the presence of iron in $Fe_2(MoO_4)_3$ enables a higher turnover frequency.

Hence, novel approaches are required that allow following the structural changes in $Fe_2(MoO_4)_3$ focusing specifically on the iron coordination sphere under operating conditions. In this respect, ^{57}Fe Mössbauer spectroscopy is very powerful. For instance, Jirak et al. explored the magnetic behavior of $Fe_2(MoO_4)_3$ by temperature-dependent Mössbauer spectroscopy and deduced a possible spin arrangement for Fe-O-Mo-O-Fe [12]. In another work by Dürl et al. [13], the defect density of $Fe_2(MoO_4)_3$ was varied using ball milling (BM). Ex situ Mössbauer spectra unraveled that two different types of defects were introduced associated with a higher performance. However, after longer application, defects were healed, and the material behaved similarly to the catalyst prior to BM [13]. This underlines, on the one hand, the high sensitivity for local changes by Mössbauer spectroscopy and, on the other hand, the necessity of in situ and operando experiments to follow changes in defect density and catalytic performance at the same time.

So far, very few in situ Mössbauer spectroscopy studies have been performed on iron molybdate, focusing mostly on methanol. Carbucicchio and Trifirò performed in situ measurements for stoichiometric $Fe_2(MoO_4)_3$ and $Fe_2(MoO_4)_3$ with an excess of MoO_3 (35%, namely, Mo:Fe = 1.8) under reductive conditions in CH_3OH/N_2 [14]. Thereby, the catalyst was first subjected to the gas feed for a distinct time at ambient pressure, then the pressure was reduced to ca. 10^{-6} bar to record the spectrum (the measurement time per Mössbauer spectrum was not given). A reduction of the material occurred only at $T \geq 230$°C. At 230°C, about 25% β-$FeMoO_4$ was formed after 5 h. On the basis of further characterization as well as catalytic conversion and selectivity data, the authors concluded that in this temperature regime the diffusion of oxygen to the surface is rate-limiting [14].

Mitov et al. [15] recorded spectra under reactive (CH_3OH/air) and reductive (CH_3OH/Ar) conditions in a temperature regime of 200°C–400°C. After applying reactive conditions for a defined time, the gas flow was changed to purely Ar. Then, Mössbauer spectra were recorded for 3–4 days each. For reactive conditions, two doublets were identified in the spectra with isomer shift (IS) and quadrupole splitting (QS) values of IS = 0.21 mm s^{-1} and QS = 0.16 mm s^{-1} for the A-site and of IS = 0.10 mm s^{-1} and QS = 0.63 mm s^{-1} for the B-site [15]. While the A-site corresponds to standard parameters obtained for bulk ferric molybdate, the B-site intensity increased with temperature and increasing methanol feed during in situ conditioning. The authors assigned this doublet to a "defective" iron (III) molybdate due to the accumulation of anion vacancies, which might be the same phase as assigned later by O'Brien as P1 [8]. Reductive conditions were applied at 300°C for up to 2.5 h. After 25 min, 20% of β-$FeMoO_4$ was formed, while after 2.5 h the iron atoms were fully converted to Fe(II). (No further reduction time in between was tested). This indicates, on the one hand, that structural changes can be probed by Mössbauer spectroscopy with high sensitivity but, on the other hand, that lower photon fluxes together with the non-resonant radiation make the realization of real-time in situ/operando experiments challenging in laboratory-based Mössbauer spectroscopy.

The significant difference in the reaction toward the β-$FeMoO_4$ phase in the above-mentioned works [14, 15] might indicate the trade-off between a good signal-to-noise ratio for Mössbauer spectroscopy (optimal mass according to thin-layer approximation [16]) and a homogeneous utilization of the overall catalyst bed. Carbucicchio et al. [14] used "thin pellets" of the pristine materials (defined mass is not given), whereas Mitov et al. [15] used 20 mg_{Fe} cm^{-2}, corresponding to ca. 106 mg cm^{-2} of $Fe_2(MoO_4)_3$.

Hence, an experimental arrangement that ensures a good signal-to-noise ratio at relevant conversion with homogeneous utilization of the catalyst bed is desired, thus making SMS highly attractive. SMS is realized by using the 14.4 keV irradiation of synchrotrons with high brilliance that is used to probe an ^{57}iron borate crystal nuclear Bragg monochromator [17]. The crystal is kept close to its Néel temperature of 75.2°C and the incident angle close to Bragg reflection [18]. At the same time, the beam size is in the μm range, enabling the use of small sample volumes. To the best of our knowledge, no in situ or operando SMS study has been conducted on any catalyst during the ODH reaction so far. It is expected that SMS can give insight into the bulk structural properties of $Fe_2(MoO_4)_3$ during

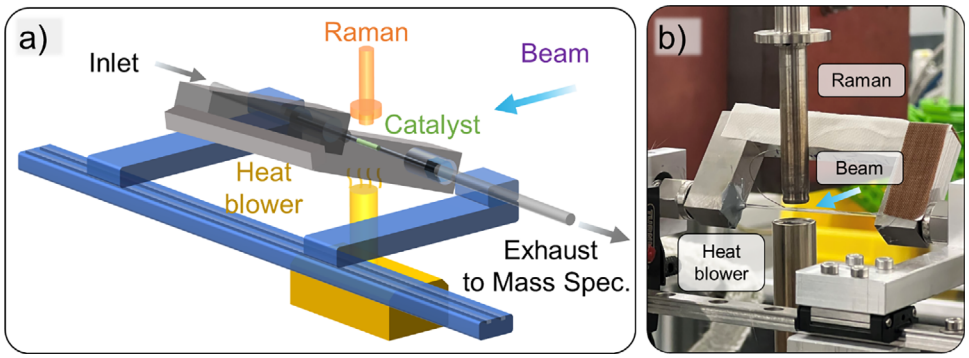

FIGURE 1 | (a) Schematic drawing of the coupled setup. (b) Picture of the operando coupled synchrotron Mössbauer spectroscopy-Raman (SMS-Raman) spectroscopy setup. The setup enables the simultaneous measurement of SMS and Raman spectra while measuring the catalytic conversion and selectivity in a mass spectrometer at temperatures up to 800°C.

the reaction. Meanwhile, as the time resolution is significantly improved in SMS, Raman spectroscopy can be coupled to provide complementary information on (sub)surface structural changes during the catalytic reaction [19], which in this context includes MoO_3 and $Fe_2(MoO_4)_3$. The simultaneous detection of both (sub)surface and bulk dynamics will be important for a detailed understanding of the overall reaction mechanism. Therefore, an appropriate synchrotron-orientated setup is required to not only capture the time-dependent $Fe_2(MoO_4)_3$ structural changes with both SMS and Raman spectroscopy but also to better mimic a practical EtOH ODH reactor.

Herein, we report the extension of a setup design widely used at synchrotron radiation sources for XAS, XRD, Raman spectroscopy, and SAXS, previously, for example, reported by Braun et al. [20] based on earlier cell designs [21, 22]. Our setup allows the coupling of SMS and Raman spectroscopy while simultaneously monitoring the catalytic gas-phase reaction using an online analysis system, herein using mass spectrometry to follow the EtOH ODH over $Fe_2(MoO_4)_3$ in an operando spectroscopic approach, allowing us to derive structure-performance relationships.

2 | Cell Design and Setup Optimization

Figure 1a depicts a scheme of the setup that is also shown in the picture taken at the European Synchrotron Research Facility (ESRF, Grenoble, France) in Figure 1b. The central part of the setup consists of a quartz capillary tube reactor that is heated by a hot air blower (Leister mini sensor kit 800 W). The temperature of the air blower was adjusted remotely for the relevant reaction conditions. A thermocouple is fixed directly at the wall of the capillary tube reactor to monitor the temperature.

To validate the setup and to find the best experimental conditions, a temperature calibration and test measurements for capillary tube size optimization were conducted. During in situ or operando experiments, the temperature is measured by a thermocouple at the outside wall of the quartz capillary. Figure 2a compares this temperature (T_{out}) with the temperature measured inside the tube reactor (T_{in}) at the same heating conditions of the gas blower, showing good agreement. The detailed temperature profile is shown in Figure S1. Based on our data, the setup enables temperature control within an experimental error of ± 5°C. As the IS changes linearly as a function of temperature in the relevant temperature regime, it can be used as an internal standard to confirm the temperature conditions. Indeed, the IS obtained for the starting compound matches the expectation for this temperature using a conventional in situ oven (both with ca. 0.24 mm s^{-1} of IS at 280°C).

SMS measurements are applied in transmission mode. Hence, the sample thickness should enable a high relative absorption while avoiding double resonance effects that might occur for thicknesses beyond the optimal values following the thin-layer approximation [16]. Based on the given enrichment factor and beam size, we tested three different diameters for the capillary tubes for data acquisition. The respective Mössbauer spectra are given in Figure 2b. In our case, quartz capillary reactors with a diameter of 1 mm and 0.01 mm wall thickness were selected for optimal detection conditions and the Mössbauer effect. Fitting analysis of these spectra is disclosed in the Supporting Information (Figure S2 and Table S1). It is noted that the optimal size of the capillary tube depends on the exact composition of the catalyst, for example, the ^{57}Fe content within the sample, but also on which other elements are present, the particle size, and bulk density.

The major difference of this setup in comparison to the one previously reported by Doronkin et al. [21] is the additional coupling to Raman spectroscopy and mass spectrometry, besides demonstrating its capability for SMS experiments. Above the quartz tube a fiberglass optic is placed that enables the coupling to Raman spectroscopy (at 532 nm excitation) in a 180° backscattering geometry simultaneously to recording SMS spectra (Figure 1b). The arrow indicates the direction of the incoming beam, and the detector is placed at the opposite site of the setup in continuation of the beam (SMS in transmission mode). The gas inlet is supplied with the transfer gas (He) in combination with EtOH vapor and/or oxygen. A syringe pump (IDL LA120) enables the injection of a controlled volume of EtOH or any other alcohol. The gas feed is remotely controlled by mass flow controllers (MFCs, Bronkhorst). Reaction conditions can be promptly changed by an automatic switching valve (VICI, EUDA-44UWE-CU). The gas outlet is connected to a mass spectrometer (Hiden Analytical) for the detection of reactants (EtOH) and products (acetaldehyde (AcH), CO_x), enabling the calculation of the catalytic conversion X and selectivity S. The Raman spectrometer (Anton Paar

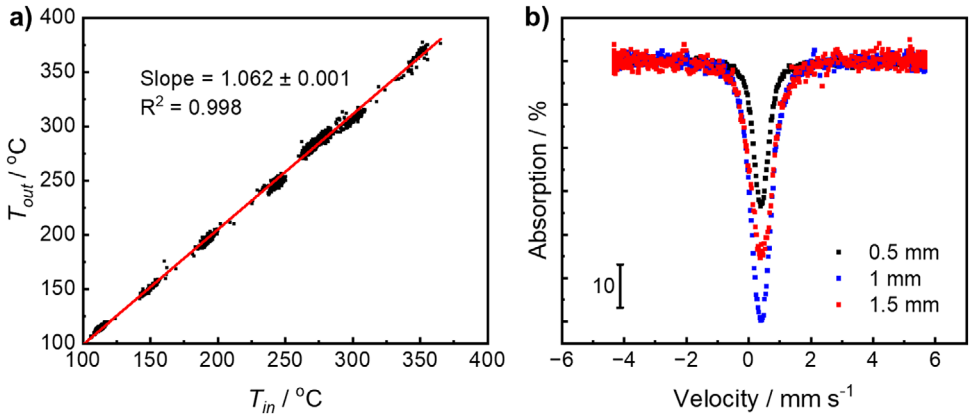

FIGURE 2 | (a) Temperature at the wall of the capillary tube reactor (T_{out}) as a function of the temperature inside the reactor (T_{in}). Two separate thermocouples were placed at the corresponding positions simultaneously. (b) Ex situ SMS measurements (at room temperature) of $Fe_2(MoO_4)_3$ (with 7% ^{57}Fe total enrichment) placed in capillary microreactors with different outer diameters.

OptoTec GmbH) enables simultaneous detection of vibrational modes associated with Mo-O-related vibrations in $Fe_2(MoO_4)_3$ and MoO_3 as described in detail below. Thus, complementary to SMS, Raman spectroscopy enables to follow structural changes of Mo-related species in the catalyst. An overview picture taken at the beamline with the assignment of components and detector is given in Figure S3.

3 | Cell Performance

In this work, we used the improved setup for coupled SMS-Raman spectroscopies to probe the role of lattice oxygen in a mixed $Fe_2(MoO_4)_3/MoO_3$ catalyst (Mo:Fe = 3) during EtOH ODH in the absence of gaseous O_2 (0.5 mol.% EtOH/He). The reason to perform such experiments under reductive conditions with our setup is not only to study the role of lattice oxygen in $Fe_2(MoO_4)_3$ when gaseous O_2 is absent but also to probe the practicality and sensitivity of the coupling setup for synchrotron-based spectroscopic experiments. The label "reductive conditions" refers to the sample's perspective, as EtOH ODH under these conditions will cause a reduction of the metals in the sample over time. Prior to this, the catalyst was subjected first to oxidative (10% O_2/He), then to reactive (0.5 mol.% EtOH/10% O_2/He), and finally again to oxidative (10% O_2/He) conditions.

The XRD data and scanning electron microscope (SEM) image of the initial catalyst are shown in the Supporting Information (Figures S4 and S5). In Figure 3a, the SMS results under reductive conditions are given. The main signature is a doublet with IS = 0.237 mm s^{-1}, and QS of 0.110 mm s^{-1}, representing Fe(III) high spin (HS) species (noted as D1a hereafter) in $Fe_2(MoO_4)_3$ (FMO). As suggested by Mitov et al. [15], a second doublet of Fe(III) (IS = 0.114 mm s^{-1}, QS = 0.630 mm s^{-1}, noted as D1b hereafter) connected to defective FMO is also considered in the fitting analysis. This second doublet D1b, however, has only a minor contribution during the reduction period. With further exposure to the reductive conditions, two more doublets appear (D2a: IS = 0.858 mm s^{-1}, QS = 0.920 mm s^{-1}; D2b: IS = 1.006 mm s^{-1}, QS = 1.342 mm s^{-1}), which are characteristic for β-$FeMoO_4$ [15, 23]. Considering a reaction according to the Mars-van Krevelen mechanism, lattice oxygen participates in the EtOH ODH reaction, while oxygen from the gas feed replenishes the vacancies in the bulk of the catalyst [15]. As no gaseous oxygen is provided under reductive conditions, Fe(III) is reduced to Fe(II), as the oxygen vacancies remain and even increase in concentration with the progress of the reaction [14, 24, 25].

The intensity of the D1b doublet remains small under all conditions, indicating that exposure to reductive conditions leads to the transformation of ferric molybdate to ferrous β-$FeMoO_4$ (spectra F in Figure 3a, enlarged spectra is shown in Figure 3b) and MoO_2 (not visible in SMS). The formation of MoO_2 was confirmed by operando coupled Raman/XRD analysis for $Fe_2(MoO_4)_3$ as starting material [26]. Fitting details of each of the above-mentioned spectra are shown in Figure S6. The SMS contour mapping converted from the same time span is shown in Figure 3c. A pronounced time-dependent change can be observed, further indicating a gradual appearance of Fe(II) species after around 30 min of time on stream under reductive conditions.

Compared to operando XAS that gives an averaged signal of all iron species and XRD that is limited to crystalline phases, SMS can directly probe the different surroundings of iron atoms [20], which helps to understand the role of Fe in $Fe_2(MoO_4)_3$ during EtOH ODH. Thus, both methods (SMS, Raman) coupled in this work are capable of detecting amorphous and crystalline contributions. While SMS is sensitive to the bulk structure, Raman spectroscopy provides information on the structure of the (sub)surface region of the catalyst. Here, Raman spectra are dominated by the crystalline phases of $Fe_2(MoO_4)_3$ and MoO_3 due to their large cross-sections. Figure 3d shows the Raman spectra at elevated temperatures under oxidative (top panel) and reductive conditions (bottom panel). The feature with the largest intensity of iron molybdate at 782 cm^{-1} originates from asymmetric stretching of MoO_4 in crystalline $Fe_2(MoO_4)_3$ [27], while the presence of crystalline MoO_3 is characterized by a sharp feature at 820 cm^{-1} resulting from corner-linking Mo-O vibrations [28]. A detailed list of features observed in Raman spectroscopy is given in Table S2. The products of the reduction, that is, $FeMoO_4$ and MoO_2, are not detected at this excitation wavelength (bottom panel), due to their low Raman cross-sections [29, 30]. Nonetheless, the Raman intensities at 820 and 782 cm^{-1} can

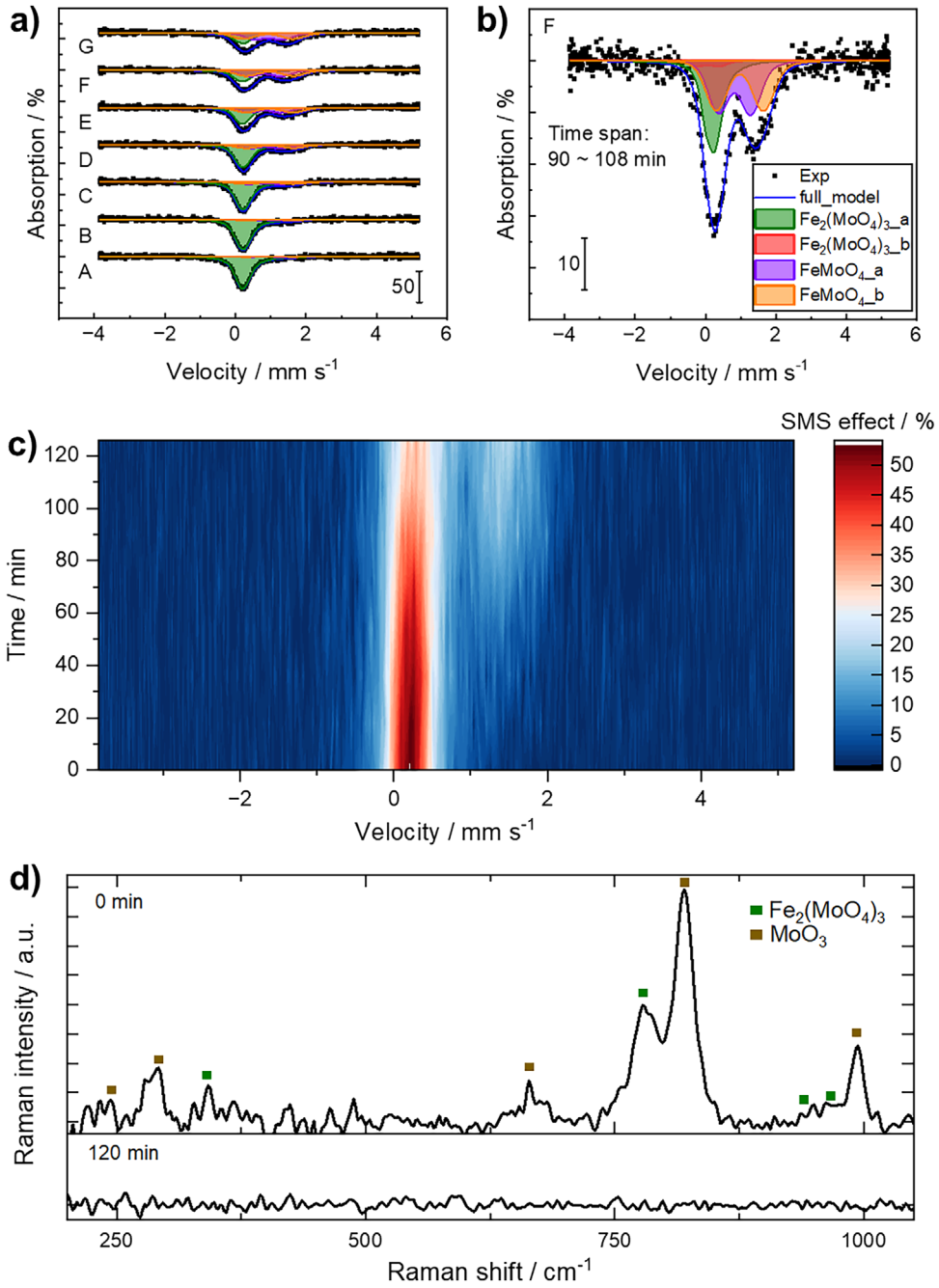

FIGURE 3 | (a) Mössbauer spectra recorded under reductive conditions at 280°C. Reactant flow: 0.5 mol.% EtOH/He (total gas flow: 90 mL min^{-1}). The time span for the experiments under reductive conditions is ca. 120 min. SMS spectra are recorded every 2 min, each fitted spectrum displayed in (a) is a sum of nine individual SMS spectra (shown as spectra A to G). (b) Representative fitting analysis of an individual spectrum under reductive condition (spectrum F in a), see Figure S6 for the other individual spectra. The color code of fitting species is the same for (a, b). (c) Contour mapping of the SMS spectra as a function of reduction time. (d) Raman spectra (at 532 nm excitation) after a 30 min exposure to oxidative conditions (10% O_2/He, total gas flow: 100 mL min^{-1}, time = 0 min) and after a 120 min exposure to reductive conditions. Signatures associated with iron molybdate (green) and MoO_3 (brown) are highlighted.

be used as an indicator for the degree of reduction during the experiment.

The results of our coupled operando SMS-Raman spectroscopic experiments are shown in Figure 4. Figure 4a depicts a schematic diagram of the commonly accepted Mars-van Krevelen type reaction mechanism and is used here to illustrate the different operation conditions. At the beginning of the experiment, oxidative and then reactive conditions were applied in succession to verify the catalyst's activity toward EtOH ODH at 280°C (noted as oxidative 1 (light purple) and reactive (green) in Figure 4a, respectively). During reactive conditions, SMS fitting analysis (Figure 4b) reveals mostly D1a (98%) Fe(III) (HS) species (noted as $Fe_2(MoO_4)_3$ site a in Figure 4b). Details of the fitting analysis are provided in Table S3. Accordingly, the D1b feature shows an intensity of around 2%. Except for the first 15 min, where the EtOH

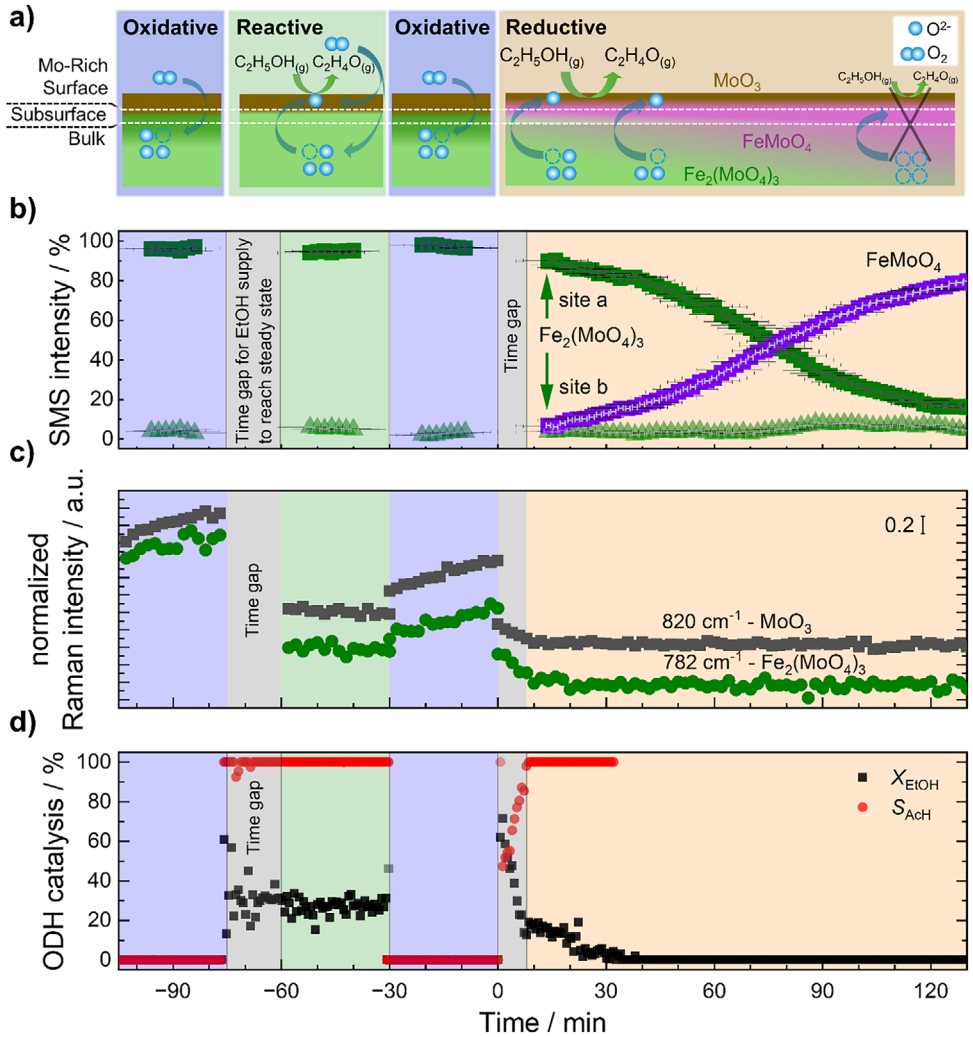

FIGURE 4 | (a) Scheme illustrating the catalyst changes for the applied gas-phase conditions. Temporal evolution of iron-related bulk phases as determined by (b) SMS incremental analysis and (c) 532 nm Raman spectroscopic bands under different gas-phase conditions at 280° C. The SMS analysis only contains the data under steady-state conditions. The continuous evolution of iron signatures over time is provided in Figure S9. (d) Conversion of EtOH (X_{EtOH}) and selectivity toward acetaldehyde (S_{AcH}) as derived from online mass spectroscopy. For $X_{EtOH} = 0$, S_{AcH} is not plotted since it is not defined mathematically. Background color code: Reactive conditions: 0.5 mol.% EtOH/10% O_2/He (green), oxidative conditions: 10% O_2/He (light purple), reductive conditions: 0.5 mol.% EtOH/He (light orange) and waiting time for the EtOH supply to reach steady state (grey). The time zero (0 min) is defined as the starting point of the reductive conditions. Reactive and oxidative conditions are part of the catalyst pre-treatment. Raman signals are normalized based on time zero (0 min).

partial pressure increases toward its steady-state value (grey region in Figure 4), online mass spectrometry reveals a steady EtOH ODH reaction with a conversion X_{EtOH} and selectivity toward acetaldehyde S_{AcH} of around 27% and 100% (Figure 4d), respectively. As expected by the low catalyst loading, the catalytic performance is smaller compared to previous results (ball milling $Fe_2(MoO_4)_3$—5 vol% EtOH, 10 vol% O_2, 85 vol% He, total volume flow: 20 mL STP min^{-1}) [3]. But more importantly, with a 100% ODH selectivity, all structural changes observed by SMS and Raman spectroscopy can be attributed to the formation of acetaldehyde.

To allow for the catalyst to return to its original state before being exposed to reductive conditions, the setup was firstly switched to oxidative conditions (light purple region in Figure 4, noted as oxidative 2) for another 30 min. The activity and selectivity of the catalyst dropped immediately to zero in the absence of EtOH, indicating the possibility of fast switching between reactive and oxidative conditions. During both types of oxidative regimes, almost all iron atoms were associated with $Fe_2(MoO_4)_3$, with D1b making only a marginal contribution. Considering the assignment of D1b to a defective iron molybdate by Mitov et al. [15], its disappearance under oxidative conditions seems reasonable, as any defects being formed during reactive conditions should be healed in the presence of oxygen from the gas feed, resulting in the dominance of the main iron molybdate signal D1a. In terms of Raman features, the intensities of the MoO_3 and $Fe_2(MoO_4)_3$ features are almost constant under reactive conditions (Figure 4c) but increase over time under oxidative conditions. This observation is associated with oxidation of the molybdenum species in the upper layers of the catalyst after being reduced during the ODH reaction, indicating their participation in EtOH ODH. Moreover,

the Raman intensity decreases upon exposure to EtOH, which is caused by reduction of the (sub-)surface of the catalyst, while there is no indication for bulk Fe reduction from SMS analysis. Based on the Raman and SMS results and the consistency with a Mars-van Krevelen mechanism, lattice oxygen is directly involved in the EtOH ODH reaction, while gas-phase oxygen replenishes the anion vacancies created in the catalyst under reactive conditions (Figure 4a).

As mentioned before, for proof of principle of the capabilities of the coupled SMS-Raman setup, the discussion in this work focuses on reductive conditions. Each fitted SM spectrum represents the overlay of nine individual 2-min spectra. Figure S7 shows the mean value and standard deviation obtained for each of these overlays. The largest standard deviation can be found in the velocity region where the ferrous iron signatures appear and it is most pronounced for the time span between 54 and 72 min.

Figure 4a illustrates the changes of the catalyst during ODH based on the Mars-van Krevelen mechanism. Note that under reductive conditions there is an increasing gradient of oxygen depletion that starts at the surface and progresses further into the bulk. Setting $t = 0$ min as the onset of the reductive conditions (light orange region), Fe(II) species (D2a and D2b in Table S4, representing β-$FeMoO_4$) start to appear in SMS, and their signals steadily increase in intensity over time. The Raman bands, on the contrary, show a sudden (within ca. 8 min) drop in intensity, as a consequence of the reduction of the (sub)surface region of the catalyst, which results in a decrease in X_{EtOH} from about 60% to 18% and an increase in S_{AcH} from 50% to 100% for S_{AcH}. Considering the time dependent behaviour of the EtOH partial pressure (Figure S8) this time window can be associated with transient conditions, where the system is about to reach its steady state. As visible in Figure S8, this transition period leads to a more pronounced change in X_{EtOH} and S_{AcH} under reductive conditions rather than reactive conditions. When reaching constant gas-phase conditions, the ODH reaction toward acetaldehyde proceeds under reductive conditions at a slightly lower conversion rate compared to reactive conditions. The remaining activity is attributed to the consumption of lattice oxygen [25].

With ongoing catalyst reduction, a further decrease of the Raman intensities is detected until a minimum is reached after about 10 min for MoO_3 and 20 min for $Fe_2(MoO_4)_3$. Within this period, iron molybdate is able to provide lattice oxygen to self-oxidize the surface layers, enabling further reaction. Within this time interval (8 to 20 min), X_{EtOH} gradually decreases to 8%. Notably, from the SMS fitting analysis only 13.5 % of iron was transferred to the ferrous state, after 20 min. After 30 min of reduction, the EtOH ODH activity is negligible. We attribute this drop to the diffusion limitation of lattice oxygen from the bulk to the surface of the catalyst when the catalyst contains less than 83.3 % of $Fe_2(MoO_4)_3$ or more than 16.7 % of β-$FeMoO_4$.

Moreover, we have also checked the reversibility of the material's reduction. After 120 min under reductive conditions, the catalyst contains 80 % of ferrous β-$FeMoO_4$. Applying a re-oxidation protocol at 350°C, most but not all of the iron is converted back to the ferric state associated with $Fe_2(MoO_4)_3$ D1a and D1b (in sum 88 %). Related Mössbauer spectra are shown in Figure S10.

Overall, the operando coupled SMS-Raman spectroscopic results confirm the necessity of the presence of Fe(III) species for an efficient EtOH ODH reaction, and illustrate that residual ODH performance is reached when the sensitivity of Raman spectroscopy fades based on the conversion of iron(III) molybdate to β-$FeMoO_4$ and MoO_2 at the (sub)surface [26, 31], while SMS reveals the structural changes of the bulk.

Summarizing, the setup presented in this work is suited to study the structural dynamics of catalytic reactions by simultaneous detection of structural changes of the bulk (SMS) and (sub-)surface (Raman). Furthermore, it allows to develop structure-property correlations, by time-dependent monitoring of spectroscopic signatures and their relation to the catalytic performance.

4 | Conclusions

The present study demonstrates the feasibility of our setup for measuring time-dependent in situ and operando synchrotron-based Mössbauer spectroscopy (SMS) coupled with Raman spectroscopy and on-line mass spectrometry. The potential of the coupled SMS-Raman approach was illustrated for the ODH of EtOH over an $Fe_2(MoO_4)_3/MoO_3$-mixture as a catalyst during reductive conditions. The coupling of both methods allows to distinguish (sub)surface and bulk properties. Based on Raman spectra, a transformation of the (sub)surface of the catalyst grains was observed after 20 min of exposure to reductive conditions, accompanied by only minor changes in the catalytic performance. In contrast, only small changes were observed by SMS at the same time as it is a bulk technique and thus less sensitive to changes in the (sub)surface region. However, SMS plays an important role in the quantitative analysis of the formation of bulk β-$FeMoO_4$ observed under further ongoing reductive conditions. In this case, the catalyst still exhibited some activity even though the overall Raman signals remained unchanged. Only when about 17% β-$FeMoO_4$ was formed, the conversion dropped to almost zero, as the diffusion of lattice oxygen became hindered. Hence, a strong dependence of the catalytic performance to the bulk phases could be observed. This study confirms the benefit of coupled operando SMS-Raman analysis to enable the time-resolved simultaneous collection of bulk and (sub)surface features. Since spectra were recorded in 2-min steps and the interplay between the surface and volume of bulk metal oxide catalysts is highly important, the setup has great potential to be applied to time-dependent operando spectroscopic experiments of other metal oxide catalysts and heterogeneous catalysts in general.

5 | Experimental Section

5.1 | Materials

Capillaries (1 mm as outer diameter, 0.02 mm wall thickness for SMS) were purchased from Hilgenberg GmbH, Germany. Ethanol (ROTIPURAN ≥ 99.8 %, CAS-No: 64-17-5) was obtained from Carl Roth.

5.2 | Catalyst Synthesis

The mixed $Fe_2(MoO_4)_3/MoO_3$-catalyst (Mo/Fe = 3) was prepared using a modification of the co-precipitation method originally described by Soares et al. [32]. A mixture (in total 8.52×10^{-4} mol) of ^{57}Fe (0.0024 g, Chemgas) and natural Fe powder (0.0452 g, Aldrich Chemicals, 99.99 %+) was dissolved in 10 mL of diluted nitric acid (the pH of the solution was adjusted to 1.5) and added dropwise (2.5 mL min^{-1}) to a solution of ammonium heptamolybdate tetrahydrate (3.64×10^{-4} mol, $(NH_4)_6Mo_7O_{24} \cdot 4\ H_2O$, Merck, extra pure) in 15 mL of H_2O. The precipitation process was then allowed to continue by stirring the suspension at 100°C for 3 h. The solid was filtered off and dried at 100°C before being calcined in air at 500°C for 10 h. X-ray powder diffraction patterns (Figure S4) and scanning electron micrographs (Figure S5) of the product clearly show the existence of two crystalline phases, $Fe_2(MoO_4)_3$ and MoO_3.

5.3 | Synchrotron Experiment

Synchrotron Mössbauer spectroscopy (SMS) measurements presented in this work were conducted at the ID14 beamline of the European Synchrotron Research Facility (ESRF) in Grenoble, France, using the transmission mode with 14.4 keV excitation energy to probe iron nuclear transitions. The beam, with a size of 10 µm (horizontal) × 5 µm (vertical), was directed at the center of a 1 mm diameter capillary to ensure uniform sample loading along the beam path. Four inclined avalanche photodiode detectors were used for signal detection. It is acknowledged that a first set of experiments (not shown) that led to an improvement of the setup and conditions was carried out at PETRA III, beamline P01.

The sample consists of 58 wt% $Fe_2(MoO_4)_3$ (with 7% ^{57}Fe total enrichment) and 42 wt% MoO_3. The typical sample bed length ranged from 5 to 6 mm, with a mass of 2 ± 0.5 mg. The distance between the gas blower and the sample was maintained at 5–6 mm. A total gas flow rate of 100 mL·min^{-1} was applied to achieve a EtOH oxidative dehydrogenation (EtOH ODH) performance comparable to previously reported values [3]. The gas replacement time is ca. 2.5 ms within the capillary tube reactor with an outer diameter of 1 mm and a wall thickness of 0.01 mm, when using a catalyst bed of 6 mm. Spectra were recorded every 2 min under various conditions.

Data analysis was carried out using the *SyncMoss* software package, which accounts for the instrumental function in fitting SMS data [33]. The experimental function was determined and verified using a single-line absorber, $K_2Mg^{57}Fe(CN)_6$, with a nominal ^{57}Fe isotope area density of 0.5 mg cm^{-2}. Calibration was performed using a standard 25 µm α-Fe foil.

SMS fitting under EtOH ODH reactive conditions was carried out by applying a D1a and a D1b site associated with ferric molybdate and its defective site, respectively; the initial parameters were fixed to the values found in literature [15, 34, 23]. For reductive conditions, besides the D1 sites, additional D2a and D2b sites are assigned for ferrous molybdate, the CS and QS values of D2 sites were allowed to change and fitted as a batch throughout the whole reductive phase while keeping the area ratio of D2a/D2b constant. We first consider Mitov et al. and Ksenofontov et al. as the references for initial D2 fitting parameters [15, 23]. Thereafter, we took the average value of fitted spectra parameters that have a more pronounced effect from the D2 site (spectra C to G in Figure 3) and used them as the initial fixed parameters for the final fitting model. SMS fitting was carried out by summing up 9 individual spectra (18 min in total), followed by an incremental fitting, which shifts the sum to the next 2-min spectra (e.g., fit#1 = 0 to 18 min, fit#2 = 2 to 20 min). Thus, we assigned the time axis error of 9 min as the average value of every 18 min fitting. The aim is to analyze the SMS data with more time resolution details.

5.4 | Raman Spectroscopy

Raman spectroscopy was performed at 532 nm laser excitation, emitted from a diode-based solid-state laser, using a commercial Raman spectrometer (Cora 5001, Anton Paar). The laser radiation and emitted Raman radiation were transferred via a high-temperature probe (Inphotonics, RPP532/12-5). The laser power at the sample location was 10 mW. The Raman radiation was dispersed by a transmission volume phase grating and detected by a charge-coupled device (CCD) detector (2048 pixels). The spectral resolution was specified by the supplier as 9 cm^{-1}. Data analysis of the Raman spectra included a dark correction.

5.5 | Mass Spectroscopy

The EtOH ODH catalytic performance was calculated based on the results from online mass spectroscopy (Hiden Analytical). During EtOH ODH, different products besides the target product acetaldehyde could be formed, where the main signal m/z is given in parenthesis: acetaldehyde (AcH, **29**), CO_x, and ethylene (**28**). Based on previous work on a FMO catalyst, the ethylene formation is insignificant [3].

Regarding the overlap of signals, EtOH and AcH both also contribute at m/z_{28}, and EtOH also to m/z_{29}, which needs to be considered in the calculations. To know the specific mass fragmentation of EtOH and AcH under relevant conditions, we performed calibration tests with pure EtOH and AcH using the same mass spectrometer and reactor setup (Table S3). As visible from Table S3, taking m/z_{31} as selective signal for ethanol only and setting its intensity to 100 %, leads to relative intensity contributions of 88 % at m/z_{29} (EtOH) and of 77.6% at m/z_{28} (EtOH). For AcH its original mass signal at m/z_{44} would overlay with CO_2. Based on this, the m/z_{29} (AcH) contribution is considered most relevant. If this intensity is set to 100%, the contribution at m/z_{28} (AcH) of 30% is most relevant for the discrimination of signal overlap with side product. Based on this, the detailed calculations are performed as follows:

Step 1: We first normalized each measured ion signal intensity by He ($m/z = 4$) to distinguish the overall pressure offset, applying Equation (1).

$$I_{corrected} = \frac{I_{measured}}{I_{He}} = \frac{I_{measured}}{\frac{m}{z}_4} \quad (1)$$

Step 2: As $m/z = 31$ is exclusively selective for the EtOH contribution, we consider the overall quantity of the as-measured

signal to the total EtOH ion signal intensity (I_{EtOH}) as given in Equation (2).

$$I_{EtOH} = \frac{m}{z}_{31} \tag{2}$$

Step 3: To obtain an intensity relevant for AcH, the relative intensity of this signal attributed to EtOH is subtracted. With the values discussed above, the acetaldehyde (AcH) ion signal intensity (I_{AcH}) can be calculated according to Equation (3):

$$I_{AcH} = \frac{m}{z}_{29} - \frac{m}{z}_{31} \times 0.88 \tag{3}$$

Step 4: For determination of the ion signal intensity of CO_x (I_{COx}), we subtract the contribution of EtOH and AcH at m/z_{28} (Equation 4):

$$I_{CO_x} = \frac{m}{z}_{28} - (I_{EtOH} \times 0.776 + I_{AcH} \times 0.3) \tag{4}$$

Based on the stoichiometric factors in the conversion of EtOH to AcH or CO_x the overall conversion can be calculated from the sum of product ion signals (corrected for the stoichiometric factors) in relation to the intensity of EtOH.

Step 5: We determine the selectivity toward AcH (S_{AcH}) as:

$$S_{AcH} = \frac{I_{AcH}}{I_{AcH} + \frac{I_{CO_x}}{2}} \tag{5}$$

Step 6: We determine the yield of AcH (Y_{AcH}) as:

$$Y_{AcH} = \frac{I_{AcH}}{I_{EtOH} + I_{AcH} + \frac{I_{CO_x}}{2}} \tag{6}$$

Step 7: Finally, we can deduce the EtOH to AcH conversion as:

$$X_{EtOH} = \frac{Y_{AcH}}{S_{AcH}} \tag{7}$$

Acknowledgments

This work was financially supported by the CRC1487 Iron, *upgraded!* (DFG funding No: 443703006). Furthermore, J.S., U.I.K., and J.-D.G. acknowledge support via the LOEWE project CleanCircles at TUD and a corresponding project of the Strategy Fund of the KIT Presidium. We acknowledge the European Synchrotron Radiation Facility (ESRF) for provision of synchrotron radiation facilities under proposal number CH-7299 and we would like to thank Dimitrios Bessas and Sergey Yaroslavtsev for assistance and support in using beamline ID14. The authors acknowledge DESY (Hamburg, Germany), a member of the Helmholtz Association HGF, for the provision of experimental facilities. A first set of experiments that let to further improvement of the setup and conditions was carried out at PETRA III, beamline P01 with the support of Ilya Sergeev and Deepak Prajapat. Beamtime was allocated for proposal I-20240188.

Open access funding enabled and organized by Projekt DEAL.

Funding

This study was supported by Deutsche Forschungsgemeinschaft (Grant 443703006), Hessisches Ministerium für Wissenschaft und Kunst (Grant LOEWE - CleanCircles), KIT (Strategy Fund), Deutsches Elektronen-Synchrotron (Grant I-20240188), and the European Synchrotron Radiation Facility (CH-7299).

Conflicts of Interest

The authors declare no conflicts of interest.

Data Availability Statement

The data that support the findings of this study are available at zenodo.org, doi: 10.5281/zenodo.21819240.

References

1. M. Bowker, R. Holroyd, and M. House, "The Selective Oxidation of Methanol on Iron Molybdate Catalysts," *Topics in Catalysis* 48 (2008): 158–165, https://doi.org/10.1007/s11244-008-9058-3.

2. A. P. V. Soares, M. F. Portela, and A. Kiennemann, "Methanol Selective Oxidation to Formaldehyde Over Iron-Molybdate Catalysts," *Catalysis Reviews* 47 (2005): 125–174, https://doi.org/10.1081/CR-200049088.

3. N. Oefner, F. Heck, and M. Dürl, "Activity, Selectivity and Initial Degradation of Iron Molybdate in the Oxidative Dehydrogenation of Ethanol," *ChemCatChem* 14 (2022): e202101219, https://doi.org/10.1002/cctc.202101219.

4. C. Brookes, M. Bowker, and P. Wells, "Catalysts for the Selective Oxidation of Methanol," *Catalysts* 6 (2016): 92, https://doi.org/10.3390/catal6070092.

5. H. Nair, J. E. Gatt, J. T. Miller, and C. D. Baertsch, "Mechanistic Insights Into the Formation of Acetaldehyde and Diethyl Ether From Ethanol Over Supported VOx, MoO_x, and WO_x Catalysts," *Journal of Catalysis* 279 (2011): 144–154, https://doi.org/10.1016/j.jcat.2011.01.011.

6. C. Hess, "Shining New Light on the Mechanism of Selective Oxidation Catalysis Using Method Development in Transient Spectroscopy," *ACS Catalysis* 15 (2025): 8005–8013, https://doi.org/10.1021/acscatal.5c01853.

7. A. Gaur, M. Stehle, and K. V. Raun, "Structural Dynamics of an Iron Molybdate Catalyst Under Redox Cycling Conditions Studied With in Situ Multi Edge XAS and XRD," *Physical Chemistry Chemical Physics* 22 (2020): 11713–11723, https://doi.org/10.1039/D0CP01506G.

8. M. G. O'Brien, A. M. Beale, S. D. M. Jacques, and B. M. Weckhuysen, "A Combined Multi-Technique In Situ Approach Used to Probe the Stability of Iron Molybdate Catalysts during Redox Cycling," *Topics in Catalysis* 52 (2009): 1400–1409, https://doi.org/10.1007/s11244-009-9324-z.

9. A. Gaur, M. Schumann, and K. V. Raun, "Operando XAS/XRD and Raman Spectroscopic Study of Structural Changes of the Iron Molybdate Catalyst During Selective Oxidation of Methanol," *ChemCatChem* 11 (2019): 4871–4883, https://doi.org/10.1002/cctc.201901025.

10. L. Schumacher, M. Radtke, J. Welzenbach, and C. Hess, "Unraveling Surface and Bulk Dynamics of Iron(III) Molybdate During Oxidative Dehydrogenation Using Operando and Transient Spectroscopies," *Communications Chemistry* 6 (2023): 230, https://doi.org/10.1038/s42004-023-01028-8.

11. S. A. Bates, "A Study to Determine the Active Site in the Oxidative Dehydrogenation of Ethanol Over Mixed Iron Molybdate Catalysts," (master's thesis, Purdue University, 2010), https://docs.lib.purdue.edu/dissertations/AAI1490624/.

12. Z. Jirak, R. Salmon, L. Fournes, F. Menil, and P. Hagenmuller, "Magnetic and Moessbauer Resonance Investigations of the Weak Ferrimagnet Iron Molybdate ($Fe_2(MoO_4)_3$)," *Inorganic Chemistry* 21 (1982): 4218–4223, https://doi.org/10.1021/ic00142a021.

13. M. Dürl, K. Sowa, and M. Panthöfer, "Insights Into the Role of Defects in $Fe_2(MoO_4)_3$ Catalysts," *Journal of Physical Chemistry C* 127 (2023): 7019–7026, https://doi.org/10.1021/acs.jpcc.3c01484.

14. M. Carbucicchio and F. Trifirò, "Surface and Bulk Redox Processes in Iron-Molybdate-Based Catalysts," *Journal of Catalysis* 45 (1976): 77–85, https://doi.org/10.1016/0021-9517(76)90057-9.

15. I. Mitov, S. Asenov, T. Tomov, and D. Klissurski, "In Situ Mössbauer Study of the Interaction of Methanol With an Iron–Molybdenum Oxide Catalyst," *Journal of Physical Chemistry C* 111 (2007): 5389–5393, https://doi.org/10.1021/jp066626e.

16. F. Grandjean and G. J. Long, "Best Practices and Protocols in Mössbauer Spectroscopy," *Chemistry of Materials* 33 (2021): 3878–3904, https://doi.org/10.1021/acs.chemmater.1c00326.

17. V. Potapkin, A. I. Chumakov, and G. V. Smirnov, "The ^{57}Fe Synchrotron Mössbauer Source at the ESRF," *Journal of Synchrotron Radiation* 19 (2012): 559–569, https://doi.org/10.1107/S0909049512015579.

18. S. Yaroslavtsev and A. I. Chumakov, "Synchrotron Mössbauer Source: Trade-off Between Intensity and Linewidth," *Journal of Synchrotron Radiation* 29 (2022): 1329–1337, https://doi.org/10.1107/S1600577522009316.

19. C. Hess, "New Advances in Using Raman Spectroscopy for the Characterization of Catalysts and Catalytic Reactions," *Chemical Society Reviews* 50 (2021): 3519–3564, https://doi.org/10.1039/D0CS01059F.

20. L. Braun, J. Spielmann, and D. E. Doronkin, "Following the Structural Changes of Iron Oxides During Reduction Under Transient Conditions," *ChemSusChem* 17 (2024): e202401045, https://doi.org/10.1002/cssc.202401045.

21. D. E. Doronkin, H. Lichtenberg, and J.-D. Grunwaldt, "Cell Designs for In Situ and Operando Studies," in *XAFS Techniques for Catalysts, Nanomaterials, and Surfaces* (Springer Nature, 2017), 75–89, https://doi.org/10.1007/978-3-319-43866-5_6.

22. J.-D. Grunwaldt, M. Caravati, S. Hannemann, and A. Baiker, "X-Ray Absorption Spectroscopy Under Reaction Conditions: Suitability of Different Reaction Cells for Combined Catalyst Characterization and Time-Resolved Studies," *Physical Chemistry Chemical Physics* 6 (2004): 3037, https://doi.org/10.1039/B403071K.

23. V. Ksenofontov, Y. G. Pashkevich, and M. Panthöfer, "$FeMoO_4$ Revisited: Crosslike 90° Noncollinear Antiferromagnetic Structure Caused by Dzyaloshinskii–Moriya Interaction," *The Journal of Physical Chemistry C* 125 (2021): 5947–5956, https://doi.org/10.1021/acs.jpcc.1c01134.

24. F. Trifirò, M. Carbucicchio, and P. L. Villa, "Catalytic Properties of Iron-Based Mixed Oxides in the Oxidation of Methanol and Olefins," *Hyperfine Interactions* 111 (1998): 17–22, https://doi.org/10.1023/A:1012612524564.

25. M. P. House, A. F. Carley, R. Echeverria-Valda, and M. Bowker, "Effect of Varying the Cation Ratio Within Iron Molybdate Catalysts for the Selective Oxidation of Methanol," *Journal of Physical Chemistry C* 112 (2008): 4333–4341, https://doi.org/10.1021/jp711251b.

26. J. Welzenbach, H. M. Wilhelm, K. Hofmann, B. Albert, and C. Hess, "Complementary and Depth-Dependent Structural Insight: A Coupled Operando Raman-X-Ray Diffraction Study on Iron Molybdate Catalysts," *Chemistry–Methods* 5 (2025): e202500095, https://doi.org/10.1002/cmtd.202500095.

27. J. Sejkora, J. Čejka, R. Malíková, A. López, Y. Xi, and R. L. Frost, "A Raman Spectroscopic Study of a Hydrated Molybdate M Ferrimolybdite, $Fe_2(MoO_4)_3{\cdot}7–8H_2O$," *Spectrochimica Acta Part A: Molecular and Biomolecular Spectroscopy* 130 (2014): 83–89, https://doi.org/10.1016/j.saa.2014.03.112.

28. L. Seguin, M. Figlarz, R. Cavagnat, and J.-C. Lassègues, "Infrared and Raman Spectra of MoO_3 Molybdenum Trioxides and $MoO_3{\cdot}xH_2O$ Molybdenum Trioxide Hydrates," *Spectrochimica Acta Part A: Molecular and Biomolecular Spectroscopy* 51 (1995): 1323–1344, https://doi.org/10.1016/0584-8539(94)00247-9.

29. M. Dieterle, "In Situ Resonance Raman Studies of Molybdenum Oxide Based Selective Oxidation Catalysts," (PhD diss., Technical University of Berlin, 2001), https://depositonce.tu-berlin.de/items/7f16c9aa-0bb2-4361-a1d8-f71c58a697dd.

30. C. Brookes, "New Insights on the Selective Oxidation of Methanol to Formaldehyde on FeMo Based Catalysts," (PhD diss., Cardiff University, 2015), https://orca.cardiff.ac.uk/id/eprint/84633/.

31. E. Söderhjelm, M. P. House, and N. Cruise, "On the Synergy Effect in MoO_3–$Fe_2(MoO_4)_3$ Catalysts for Methanol Oxidation to Formaldehyde," *Topics in Catalysis* 50 (2008): 145–155, https://doi.org/10.1007/s11244-008-9112-1.

32. A. V. Soares, M. F. Portela, and A. Kiennemann, "Iron Molybdates for Selective Oxidation of Methanol: Mo Excess Effects on the Deactivation Behaviour," *Catalysis Communications* 2 (2001): 159–164, https://doi.org/10.1016/S1566-7367(01)00026-7.

33. S. Yaroslavtsev, "*SYNCmoss* Software Package for Fitting Mössbauer Spectra Measured With a Synchrotron Mössbauer Source," *Journal of Synchrotron Radiation* 30 (2023): 596–604, https://doi.org/10.1107/S1600577523001686.

34. A. W. Sleight, B. L. Chamberland, and J. F. Weiher, "Magnetic, Mössbauer, and Structural Studies on Three Modifications of $FeMoO_4$," *Inorganic Chemistry* 7 (1968): 1093–1098, https://doi.org/10.1021/ic50064a010.

Supporting Information

Additional supporting information can be found online in the Supporting Information section.

Supporting File: 02 Supporting Information corr for Publication.pdf.